THE JOURNAL OF PHYSICAL CHEMISTRY Letters

Letter

Cite This: J. Phys. Chem. Lett. 2018, 9, 4199−4205

pubs.acs.org/JPCL

Pressure-Induced Phase Transformation and Band-Gap Engineering of Formamidinium Lead Iodide Perovskite Nanocrystals

Hua Zhu,[†] Tong Cai,[†] Meidan Que,[†] Jeong-Pil Song,[†] Brenda M. Rubenstein,[†] Zhongwu Wang,[‡] and Ou Chen*[,†]

[†]Department of Chemistry, Brown University, Providence, Rhode Island 02912, United States

[‡]Cornell High Energy Synchrotron Source, Cornell University, Ithaca, New York 14853, United States

Supporting Information

ABSTRACT: Formamidinium lead halide ($FAPbX_3$, X = Cl, Br, I) perovskite materials have recently drawn an increased amount of attention owing to their superior optoelectronic properties and enhanced material stability as compared with their methylammonium-based (MA-based) analogues. Herein, we report a study of the pressure-induced structural and optical evolutions of $FAPbI_3$ hybrid organic−inorganic perovskite nanocrystals (NCs) using a synchrotron-based X-ray scattering technique coupled to in situ absorption and photoluminescence spectroscopies. As a result of their unique structural stability and soft nature, $FAPbI_3$ NCs exhibit a wide range of band-gap tunability (1.44−2.17 eV) as a function of pressure (0−13.4 GPa). The study presented here not only provides an efficient and chemically orthogonal means to controllably engineer the band gap of $FAPbI_3$ NCs using pressure but more importantly sheds light on how to strategically design the band gaps of FA-based hybrid organic−inorganic perovskites for various optoelectronic applications.

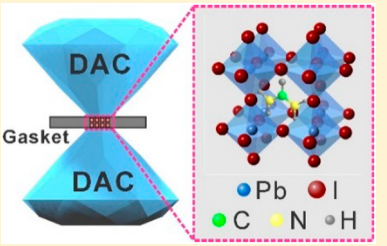

Hybrid organic−inorganic perovskites consisting of an organic cation caged within an inorganic cuboctahedral framework[1−4] have recently drawn a significant amount of attention owing to their unique crystal structure, high defect tolerances, and superior optoelectronic properties.[2,4−17] To this extent, formamidinium lead iodide ($FAPbI_3$) perovskites stand as one of the most promising candidates for optoelectronic applications among all the perovskite materials owing to their small band gap (i.e., ∼1.45 eV), balanced ionic sizes and thus high thermal and moisture stabilities, long photocarrier lifetime and diffusion length, and large optical absorption coeffcients.[7,18,19] Altogether, these properties strongly suggest that $FAPbI_3$ perovskites have the potential to become cornerstones of all future optoelectronic devices, including solar cells.[7,19−24] In addition, scaling these materials to the nanoscale sizes of colloidal $FAPbI_3$ nanocrystals (NCs) improves their properties over their bulk counterparts: NCs can be processed in solution, their band gaps may be tuned by changing particle size and shape, and NCs exhibit enhanced phase stability and mixability with other functional materials.[8,9,25] Hence the study of the structural and optical behaviors, as well as their correlations, of $FAPbI_3$ hybrid perovskite NCs is not only fundamentally important but also technologically relevant. To this end, diamond anvil cell (DAC)-based high-pressure techniques in conjunction with in situ structural and optical characterizations have recently arisen as a fast and convenient means to study, process, modify, and improve nanomaterials.[26−36] To date, various perovskite systems have been investigated using this technique at extreme pressures.[36−44] Interesting structure−property relationship diagrams of perovskite materials have been reported, including those of bulk FA-based hybrid perovskites.[37,45,46] However, such studies have yet to be extended to understanding FA-based nanoscale systems.

Herein, we present a pressure-processing study of high-quality $FAPbI_3$ hybrid organic−inorganic perovskite NCs across a wide range of pressures using a DAC. Simultaneous characterization of structural and optical properties allowed us to reveal not only the crystal phase transformations of the materials but also the structure−optical−property correlations in situ. In contrast with related bulk studies, our study shows that the $FAPbI_3$ NCs undergo a phase transition from a perfect cubic lattice of $Pm\bar{3}m$ to a cubic supercell of $Im\bar{3}$ without assuming the commonly observed orthorhombic (*Pnma*) phase before amorphization. This high structural stability combined with the low bulk modulus of $FAPbI_3$ perovskite NCs leads to the widest range of band-gap tunability of all other studied perovskite materials. Our study sheds light onto how to design band gaps of FA-based perovskite NC materials for a wide spectrum of applications.

$FAPbI_3$ hybrid perovskite NCs were synthesized using a previously published method (see the Experimental Section and the Supporting Information (SI)).[9] Figure 1A shows the absorption and photoluminescence (PL) spectra of the $FAPbI_3$ NCs. Transmission electron microscopy (TEM) measurements show that the $FAPbI_3$ NCs have a cubic shape with an average edge length of 19.0 ± 3.4 nm (Figure 1B and Figure S1). The high-resolution TEM (HR-TEM) measurements

Received: June 13, 2018
Accepted: July 10, 2018
Published: July 10, 2018

DOI: 10.1021/acs.jpclett.8b01852
J. Phys. Chem. Lett. 2018, 9, 4199−4205

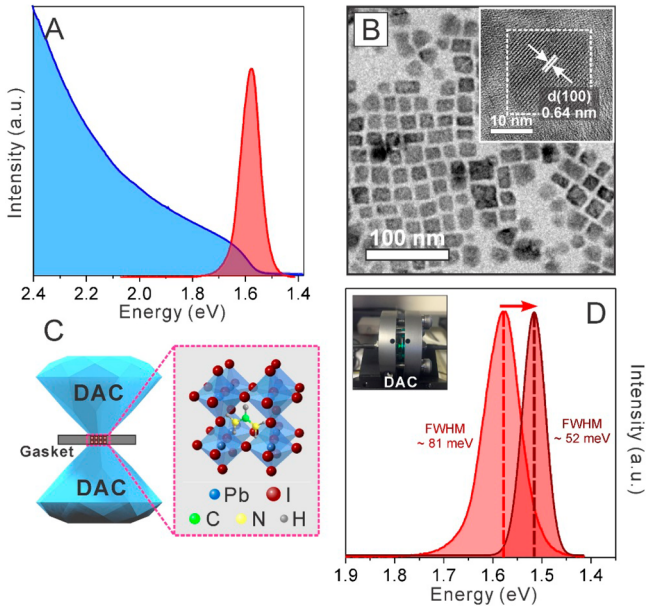

Figure 1. (A) Absorption (blue) and PL (red) spectra of the $FAPbI_3$ perovskite NCs in toluene. (B) Typical TEM image of the $FAPbI_3$ perovskite NCs as a cubic shape with an average edge length of 19.0 ± 3.4 nm. Inset shows a high-resolution (HR)-TEM image of one particle. (C) Schematic of $FAPbI_3$ NCs inside a DAC. (D) PL spectra of the NCs in solution (red line) and in the DAC (dark red line). Inset shows a DAC loaded with NCs.

clearly reveal the atomic lattice fringes with a d spacing of 6.4 Å, corresponding to the (100) plane of the $FAPbI_3$ cubic crystal phase (space group: $Pm\bar{3}m$).[3] The as-synthesized $FAPbI_3$ NC−toluene suspension was slowly dried and loaded into a DAC. The PL peak was red-shifted ~71 meV (~37 nm) and became ~35% narrower (81 vs 52 meV) than that of the solvent-dispersed NCs, indicating that the reabsorption and re-emission processes occur within a densely packed NC film.[47]

To characterize the crystal phase evolution of $FAPbI_3$ NCs under pressure, HR synchrotron-based wide-angle X-ray scattering (WAXS) patterns were collected upon applying pressure. Figure 2 shows a series of WAXS patterns collected during a pressure cycle of 0−13.4 GPa. At ambient pressure, $FAPbI_3$ NCs had a perfect cubic crystal phase (space group: $Pm\bar{3}m$) with a lattice constant of a = 6.351 Å (Figure 2H, Figure S2, and Table S2), in good agreement with HR-TEM measurements (Figure 1B, inset). Upon compression, the cubic phase remained stable up to ~0.6 GPa, whereas all of the WAXS peaks shifted to larger angles, indicating a uniform shrinkage of the atomic lattice. When the pressure reached 0.6 GPa, two additional scattering peaks emerged at q values of 15.9 and 18.8 nm^{-1} (Figure 2E and Figure S4), which were well assigned to the (310) and (321) planes of the $Im\bar{3}$ crystal phase of $FAPbI_3$, respectively. This observation suggested that the $FAPbI_3$ NCs underwent a phase transition from $Pm\bar{3}m$ to $Im\bar{3}$, in line with previous reports on FA-based lead halide bulk crystal materials.[45] The emergent tilting of $[PbI_6]^{4-}$ octahedra resulted in an enlarged (2 × 2 × 2) supercell lattice (Figure

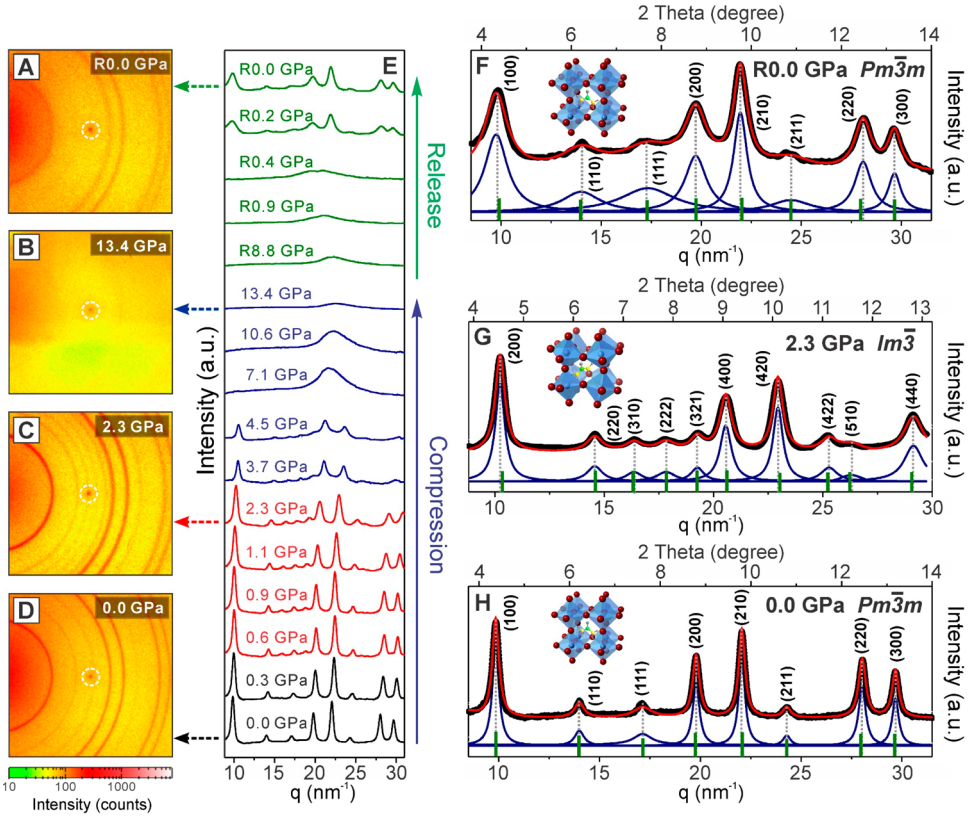

Figure 2. (A−D) Integrated 2D WAXS patterns of $FAPbI_3$ NCs during a sequential compression−decompression cycle. The white dashed circles are noise signals on the detector. The signal intensity is shown in the scale bar below. (E) WAXS patterns at different pressures during the compression and decompression processes. (F−H) Integrated WAXS spectra with calculated Bragg reflection positions at R0.0 (after decompression), 2.3, and 0.0 GPa, respectively. The green bars show the calculated Bragg reflection positions of each phase. At 0.0 and R0.0 GPa, $FAPbI_3$ NCs show a perfect cubic $Pm\bar{3}m$ crystal phase. At 2.3 GPa, NCs show a cubic supercell $Im\bar{3}$ crystal phase.

DOI: 10.1021/acs.jpclett.8b01852
J. Phys. Chem. Lett. 2018, 9, 4199−4205

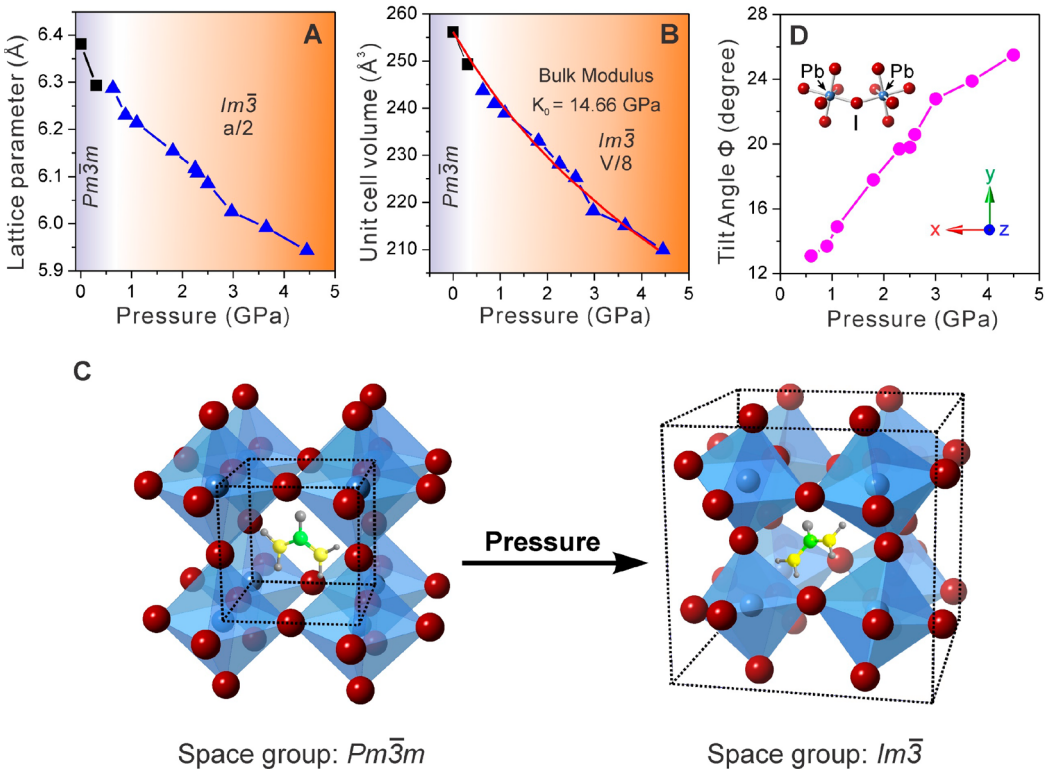

Figure 3. Plots of the evolution of the $FAPbI_3$ structure as a function of pressure. (A) Lattice parameter evolution during pressure. Lattice parameters are normalized (a for $Pm\bar{3}m$ crystal phase (square) and $a/2$ for $Im\bar{3}$ crystal phase (triangle)) for a fair comparison. (B) Evolution of normalized unit-cell volumes. The red line is a fitted curve using the second-order Birch−Murnaghan equation of state, giving a bulk modulus of 14.66 GPa. (C) Unit-cell schematics of $FAPbI_3$ perovskite NCs with $Pm\bar{3}m$ (left panel) and $Im\bar{3}$ (right panel) crystal structures. The $[PbI_6]^{4-}$ octahedron was tilted along the [111] cubic direction in the $Im\bar{3}$ phase. Black dotted lines indicate the unit-cells. (D) Octahedral tilt angle evolution as a function of pressure.

S3) as compared with the initial $FAPbI_3$ cubic phase ($Pm\bar{3}m$).[4,45] Upon further compression, all of the scattering peaks red-shifted while maintaining the crystallographic relationship, indicating a preservation of the $Im\bar{3}$ phase (Figure 2E). In contrast with the $MAPbI_3$ NCs and $FAPbBr_3$ bulk crystal cases, no subsequent phase transition to the highly distorted orthorhombic phase (space group: *Pnma*) was observed over the pressure range of 2−3 GPa in this study (Figures S4−S7 and Tables S3−S6). The WAXS pattern at 2.3 GPa is shown in Figure 2C as one example. All of the scattering peaks are highly symmetric and do not show any noticeable splitting (Figure 2G). The pattern can be refined into a perfect cubic phase ($Im\bar{3}$), giving rise to a measured supercell lattice constant of a = 12.22 Å (i.e., $a/2$ = 6.11 Å) (Figure S6 and Table S5). This improved structural stability is most likely caused by four short hydrogen bonds (NH···I) formed between the FA^+ cation and I^- anions of the inorganic perovskite sublattice within individual NCs.[3,48−50] When the applied pressure surpassed 3 GPa, the WAXS patterns started to show a diffuse background and decreased scattering intensity with a broadening peak profile, indicating the onset of a partial amorphization process, as observed in other perovskite NC systems.[40,45,51−53] When the pressure reached 7.1 GPa, the perovskite structure totally disappeared, resulting in complete amorphization, as indicated by a single broad scattering feature at q values of ∼22−25 nm^{-1} in the WAXS patterns (Figure 2E). Upon release of pressure, the amorphous state was preserved until the pressure was below 0.4 GPa (Figure 2A). A complete pressure removal induced a rapid perovskite crystallization to the original cubic phase (R0.0 GPa, $Pm\bar{3}m$, Figure 2E,F). Notably, all of the scattering peaks were broader than those in the original WAXS pattern (Figure 2F), indicating a partial loss of crystallinity of the $FAPbI_3$ NCs. TEM measurements of the pressed sample confirmed our hypothesis, which showed no significant changes in particle size and shape (Figures S8 and S9).

To understand pressure-induced atomic motions during the phase transitions, we conducted a detailed structural analysis of $FAPbI_3$ NCs before amorphization. Within the pressure range of 0−0.6 GPa, $FAPbI_3$ NCs showed a perfect cubic structure, which maintained the Pb−I−Pb bond angle of 180°. The shrinkage of the lattice parameter and thus the decrease in unit-cell volume was a direct consequence of Pb−I bond contraction (Figure 3A,B). The continuous increase in pressure led to a distorted perovskite structure (space group: $Im\bar{3}$) with a $[PbI_6]^{4-}$ octahedral tilt of equal magnitude about all three Cartesian axes (Glazer notation: $a^+a^+a^+$, Figure 3C and Figure S10).[54] The tilting angle (Φ) with respect to the [111] crystal axis increased from 13.1° at 0.6 GPa to 25.5° at 4.5 GPa (Figure 3D and Table S7). This experimental observation was consistent with the high rigidity of the $[PbI_6]^{4-}$ octahedral units as compared with the $[FAI_{12}]^{11-}$ cuboctahedral ones.[45] On the basis of our structural assignment, the volumetric compression as a function of pressure gave a bulk modulus (K_0) of 14.66 GPa via fitting of the second-order Birch−Murnaghan equation of state (Figure 3B), comparable to previous reports for $MAPbI_3$.[37,40] Note that this bulk modulus (K_0) of $FAPbI_3$ NCs is significantly lower than

DOI: 10.1021/acs.jpclett.8b01852
J. Phys. Chem. Lett. 2018, 9, 4199−4205

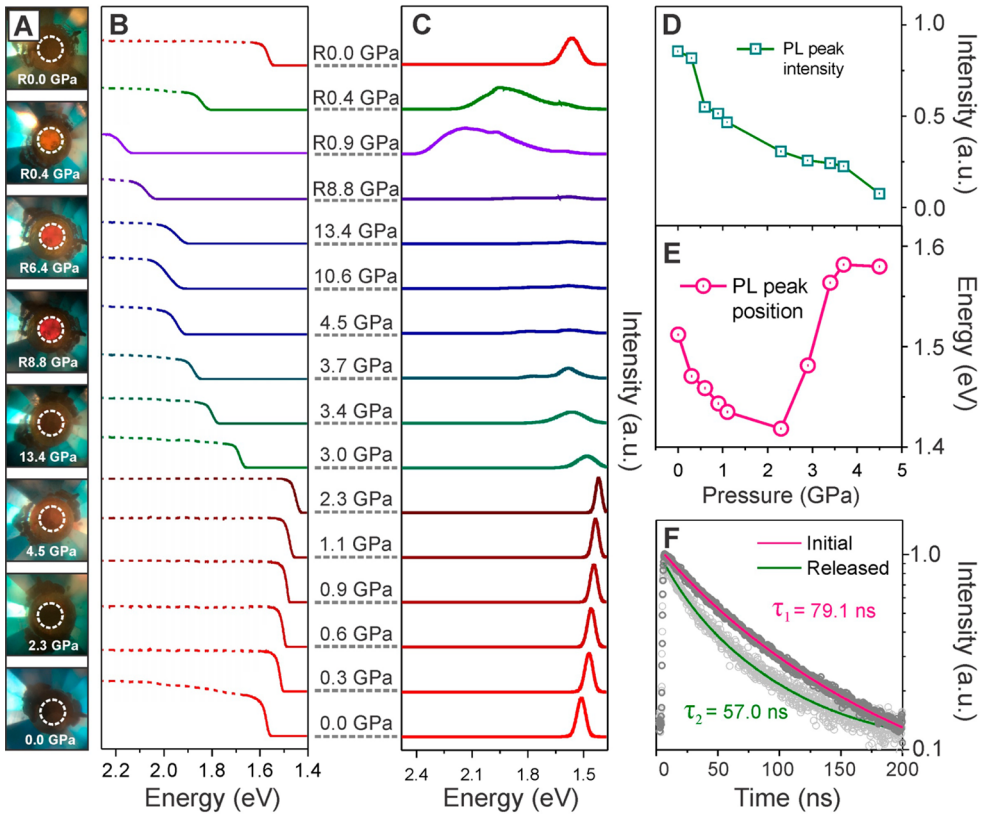

Figure 4. (A) Series of photographs of $FAPbI_3$ NCs in a DAC at different pressures. (B) Absorption and (C) PL evolutions during the pressure cycle. Dashed lines indicate the possible signal saturation. (D) PL peak intensity evolution before complete amorphization. The PL intensity shows a continuous decrease with increasing pressure. (E) PL peak position evolution before complete amorphization. The peak position first red-shifts, then blue-shifts, and finally remains at constant value. (F) PL lifetime decay curves of the $FAPbI_3$ NCs before and after pressure treatment.

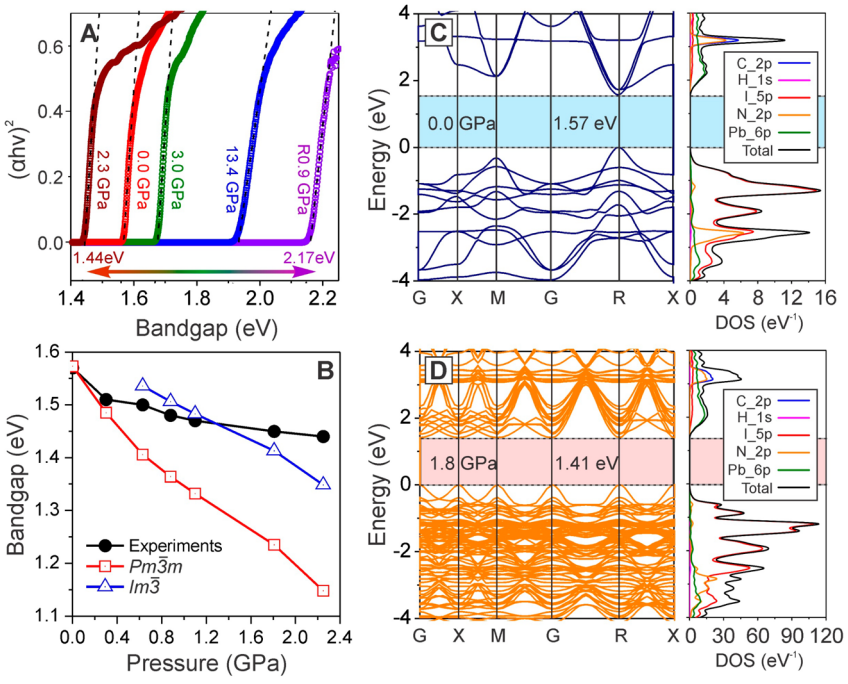

Figure 5. (A) Tauc plots of $FAPbI_3$ NCs at different pressures showing the absorption onset. (B) Band-gap evolution based on experimental data and DFT calculations for both the $Pm\bar{3}m$ and $Im\bar{3}$ (corresponding to U = 1.2 and 0 eV) crystal phases. (C,D) Calculated band structures of $FAPbI_3$ NCs at 0.0 and 1.8 GPa (left panels) and the corresponding DOS (right panels), respectively.

that of all-inorganic perovskites, such as $CsPbBr_3$, and $CsPbI_3$.[26,51] The soft nature of $FAPbI_3$ NCs results in a larger distortion of the Pb−I−Pb bond and hence a smaller coupling between Pb 6p orbitals and I 5p orbitals under pressure, which,

DOI: 10.1021/acs.jpclett.8b01852
J. Phys. Chem. Lett. 2018, 9, 4199−4205

in principle, would enable a wide range of tunability for the pressure-engineered band gap of $FAPbI_3$ NCs.[37]

To understand the behavior of the optical properties of $FAPbI_3$ NCs under high pressure, we performed in situ absorption and PL measurements during the pressure cycle. The entire optical profile progression was strongly coincident with the pressure-induced phase transition and amorphization processes of the $FAPbI_3$ NCs. In detail, continuous red shifts of both absorption (from 1.57 to 1.44 eV) and PL spectra (from 1.51 to 1.42 eV) were observed in the pressure range of 0−2.3 GPa (Figure 4A−E). This can be attributed to the Pb−I bond contraction, which leads to a greater orbital wave function overlap, thus narrowing the band gap.[37,43] Upon further compression, the absorption band and PL peak started blue-shifting, whereas the PL intensity decreased dramatically and became nearly undetectable when the pressure was increased above ∼5 GPa (Figure 4C−E). The decrease in PL intensity was attributed to the pressure-induced band gap widening, which creates deep intraband trap states with fast nonradiative relaxation pathways.[40,45] Interestingly, during the decompression process, the absorption band kept blue-shifting until the pressure was released to 0.9 GPa, where a broad PL peak at ∼2.1 eV emerged (Figure 4C) while retaining the amorphous phase of NCs (Figure 2E). Although the origin of this amorphous state PL remains unclear, it is likely related to a short-range order of highly tilted $[PbI_6]^{4-}$ octahedra inside the amorphous $FAPbI_3$ NCs. When the pressure was released below ∼1.0 GPa, the NC surface states became less strained with fewer defects and shallower surface-related exciton trap states,[26,55,56] resulting in an enhanced amorphous state emission, as we observed. Further releasing pressure resulted in reversible red shifts of both the absorption feature and the PL peak, and the PL peak center finally bounced back to 1.56 eV when the pressure was completely removed (Figure 4B,C). The final PL profile exhibited higher energy (∼50 meV), a broader line width (∼100%), and shorter-lived charge carriers (lifetime of 57.0 vs 79.1 ns; see the details in Table S1) than the initial PL of the $FAPbI_3$ NCs before pressurization (Figure 4C,F). These observations can be explained by the poor crystallinity, less ordered surface atoms, and ligand states of the final NCs after pressure-treatment, consistent with the WAXS data sets (Figure 2E,F). TEM characterizations of the pressed $FAPbI_3$ NCs did not show significant alterations in particle sizes and shapes (Figures S8 and S9), supporting our explanation.

Because band-gap engineering of perovskite materials is essential for photovoltaic and other applications, we performed a detailed band-gap analysis using Tauc plot fitting of the linear region of the absorption band spectra and density functional theory (DFT) band structure calculations as a function of applied pressure (Figure 5, Figures S11−S13).[57] Figure 5A shows the band-gap evolution determined by a Tauc plot at different pressures. Remarkably, the pressure-tuned band gap spanned a significantly wider range (∼0.7 eV) than all other reported perovskite materials across different length scales (Figure 5A and Figure S12).[37,39,41,43−45,51] Although the band gap in an amorphous phase cannot be quantitatively determined, detailed band structures were calculated using first-principles DFT calculations for the two crystal phases (i.e., $Pm\bar{3}m$ and $Im\bar{3}$). The density of states (DOS) calculation results clearly revealed that the valence band (VB) mainly consists of I 5p orbitals, whereas the conduction band (CB) is dominated by Pb 6p orbitals (Figure 5C,D and Figure S13). Consequently, the high-pressure-induced band-gap evolution was dictated by the structural behavior of the $[PbI_6]^{4-}$ octahedral subunits. Below 0.6 GPa, homogeneous contraction of $[PbI_6]^{4-}$ octahedra resulted in a continuous shrinkage of the Pb−I bond, directly promoting the two p orbitals' overlap, thus narrowing the band gap efficiently (Figure 5B and Figure S13). When the crystal phase transitioned to $Im\bar{3}$, drastic $[PbI_6]^{4-}$ octahedral tilt resulted in reducing the Pb−I−Pb bond angle from 180°. This off-aligned Pb−I−Pb bond diminished the symmetry match between the Pb 6p orbital and the I 5p orbital. As a result, a slower band-gap narrowing process was observed from both the Tauc plot analysis and DFT calculations (Figure 5B). Above 3.0 GPa, the subsequent structural amorphization of $FAPbI_3$ NCs induced a large band-gap increase. Although the physical and thus the electronic structures of the amorphous state of $FAPbI_3$ NCs cannot be precisely determined, significant $[PbI_6]^{4-}$ octahedral tilt and crystal domain reduction would reasonably be responsible for the further band-gap widening.

In conclusion, we probed the pressure-induced structural and optical property evolutions of $FAPbI_3$ hybrid organic−inorganic perovskite NCs within a pressure cycle of 0−13.4 GPa. The $FAPbI_3$ NCs underwent a phase transition from a cubic $Pm\bar{3}m$ to a cubic supercell $Im\bar{3}$ in the pressure range of 0−3 GPa, followed by an amorphization process. Evolutions of the absorption and PL profiles of the $FAPbI_3$ NCs as a function of pressure show a strong correlation with the crystal structure changes, consistent with the DFT band structure calculations. Importantly, the high structural stablilty with a low bulk modulus of $FAPbI_3$ NCs leads to a wide range of band-gap tunability from 1.44 to 2.17 eV, which is significantly wider than that of all other reported perovskite materials within a similar range of pressure cycle. Such a high band-gap engineering capability is crucial in optoelectronic applications of hybrid organic−inorganic perovskite NC materials. Our study provides important design rules for generating FA-based hybrid perovskite materials with optimized structure-determined optical properties in and even beyond optoelectronic applications.

EXPERIMENTAL SECTION

$FAPbI_3$ NCs were synthesized using a modified literature method.[9] Synchrotron-based WAXS measurements[28] and in situ absorption (Abs) and PL characterizations were performed at the B1 station of Cornell High Energy Synchrotron Source (CHESS), Cornell University. A diamond anvil cell (DAC) was used for the high-pressure experiment. In situ PL measurements were performed through the DAC using an Ocean Optics and Thorlabs setup, in which the sample was illuminated by a 365 nm diode light source and the signal was collected by Ocean Optics spectrometer (USB2000+). In situ Abs measurements were performed through the DAC using an Ocean Optics setup, in which the sample was illuminated by white-light source from Thorlabs (SLS201L) and the signal was collected by an Ocean Optics spectrometer (USB2000+). First-principles density functional theory (DFT) calculations were carried out based on the generalized gradient approximation (GGA) within DFT using the Quantum Espresso (QE) program. We employed the GGA+U method in accordance with the Hubbard U approach.[58,59] The calculations were performed using the Perdew−Burke−Ernzerhof (PBE) exchange-correlation functional. See the SI for experimental and computational details.

DOI: 10.1021/acs.jpclett.8b01852
J. Phys. Chem. Lett. 2018, 9, 4199−4205

■ ASSOCIATED CONTENT

Supporting Information

The Supporting Information is available free of charge on the ACS Publications website at DOI: 10.1021/acs.jpclett.8b01852.

Additional experimental and computational details, WAXS analysis $FAPbI_3$ NCs under pressure, and band-gap calculations (PDF)

■ AUTHOR INFORMATION

Corresponding Author

*E-mail: ouchen@brown.edu.

ORCID

Hua Zhu: 0000-0003-2733-7837

Zhongwu Wang: 0000-0001-9742-5213

Ou Chen: 0000-0003-0551-090X

Notes

The authors declare no competing financial interest.

■ ACKNOWLEDGMENTS

O.C. acknowledges the support from the Brown University startup fund and IMNI seed fund. O.C. also gives thanks to the Xerox foundation. CHESS was supported by the NSF award DMR-1332208. The TEM measurements were performed at the Electron Microscopy Facility in the Institute for Molecular and Nanoscale Innovation (IMNI) at Brown University. This research was conducted using computational resources and services at the Brown University Center for Computation and Visalization.

■ REFERENCES

(1) Akkerman, Q. A.; Raino, G.; Kovalenko, M. V.; Manna, L. Genesis, Challenges and Opportunities for Colloidal Lead Halide Perovskite Nanocrystals. *Nat. Mater.* **2018**, *17*, 394−405.

(2) Han, Q. F.; Bae, S. H.; Sun, P. Y.; Hsieh, Y. T.; Yang, Y.; Rim, Y. S.; Zhao, H. X.; Chen, Q.; Shi, W. Z.; Li, G.; et al. Single Crystal Formamidinium Lead Iodide ($FAPbI_3$): Insight into the Structural, Optical, and Electrical Properties. *Adv. Mater.* **2016**, *28*, 2253−2258.

(3) Weller, M. T.; Weber, O. J.; Frost, J. M.; Walsh, A. Cubic Perovskite Structure of Black Formamidinium Lead Iodide, alpha-$[HC(NH_2)_2]PbI_3$, at 298 K. *J. Phys. Chem. Lett.* **2015**, *6*, 3209−3212.

(4) Stoumpos, C. C.; Kanatzidis, M. G. The Renaissance of Halide Perovskites and Their Evolution as Emerging Semiconductors. *Acc. Chem. Res.* **2015**, *48*, 2791−2802.

(5) Service, R. F. ENERGY TECHNOLOGY Perovskite Solar Cells Keep On Surging. *Science* **2014**, *344*, 458−458.

(6) Jeon, N. J.; Noh, J. H.; Yang, W. S.; Kim, Y. C.; Ryu, S.; Seo, J.; Seok, S. I. Compositional Engineering of Perovskite Materials for High-Performance Solar Cells. *Nature* **2015**, *517*, 476−480.

(7) Eperon, G. E.; Stranks, S. D.; Menelaou, C.; Johnston, M. B.; Herz, L. M.; Snaith, H. J. Formamidinium Lead Trihalide: a Broadly Tunable Perovskite for Efficient Planar Heterojunction Solar Cells. *Energy Environ. Sci.* **2014**, *7*, 982−988.

(8) Fu, Y. P.; Zhu, H. M.; Schrader, A. W.; Liang, D.; Ding, Q.; Joshi, P.; Hwang, L.; Zhu, X. Y.; Jin, S. Nanowire Lasers of Formamidinium Lead Halide Perovskites and Their Stabilized Alloys with Improved Stability. *Nano Lett.* **2016**, *16*, 1000−1008.

(9) Protesescu, L.; Yakunin, S.; Kumar, S.; Bar, J.; Bertolotti, F.; Masciocchi, N.; Guagliardi, A.; Grotevent, M.; Shorubalko, I.; Bodnarchuk, M. I.; et al. Dismantling the "Red Wall" of Colloidal Perovskites: Highly Luminescent Formamidinium and Formamidinium-Cesium Lead Iodide Nanocrystals. *ACS Nano* **2017**, *11*, 3119−3134.

(10) Mao, L. L.; Ke, W. J.; Pedesseau, L.; Wu, Y. L.; Katan, C.; Even, J.; Wasielewski, M. R.; Stoumpos, C. C.; Kanatzidis, M. G. Hybrid Dion-Jacobson 2D Lead Iodide Perovskites. *J. Am. Chem. Soc.* **2018**, *140*, 3775−3783.

(11) Yang, T. Y.; Gregori, G.; Pellet, N.; Gratzel, M.; Maier, J. The Significance of Ion Conduction in a Hybrid Organic-Inorganic Lead-Iodide-Based Perovskite Photosensitizer. *Angew. Chem., Int. Ed.* **2015**, *54*, 7905−7910.

(12) Fabini, D. H.; Stoumpos, C. C.; Laurita, G.; Kaltzoglou, A.; Kontos, A. G.; Falaras, P.; Kanatzidis, M. G.; Seshadri, R. Reentrant Structural and Optical Properties and Large Positive Thermal Expansion in Perovskite Formamidinium Lead Iodide. *Angew. Chem., Int. Ed.* **2016**, *55*, 15392−15396.

(13) Pool, V. L.; Dou, B.; Van Campen, D. G.; Klein-Stockert, T. R.; Barnes, F. S.; Shaheen, S. E.; Ahmad, M. I.; van Hest, M. F. A. M.; Toney, M. F. Thermal Engineering of $FAPbI_3$ Perovskite Material via Radiative Thermal Annealing and in situ XRD. *Nat. Commun.* **2017**, *8*, 14075.

(14) Lin, J.; Lai, M. L.; Dou, L. T.; Kley, C. S.; Chen, H.; Peng, F.; Sun, J. L.; Lu, D. L.; Hawks, S. A.; Xie, C. L.; et al. Thermochromic Halide Perovskite Solar Cells. *Nat. Mater.* **2018**, *17*, 261−267.

(15) Fu, Y. P.; Wu, T.; Wang, J.; Zhai, J. Y.; Shearer, M. J.; Zhao, Y. Z.; Hamers, R. J.; Kan, E. J.; Deng, K. M.; Zhu, X. Y.; et al. Stabilization of the Metastable Lead Iodide Perovskite Phase via Surface Functionalization. *Nano Lett.* **2017**, *17*, 4405−4414.

(16) Dou, L. T.; Wong, A. B.; Yu, Y.; Lai, M. L.; Kornienko, N.; Eaton, S. W.; Fu, A.; Bischak, C. G.; Ma, J.; Ding, T. N.; et al. Atomically Thin Two-Dimensional Organic-Inorganic Hybrid Perovskites. *Science* **2015**, *349*, 1518−1521.

(17) Yin, G. N.; Ma, J. X.; Jiang, H.; Li, J.; Yang, D.; Gao, F.; Zeng, J. H.; Liu, Z. K.; Liu, S. F. Enhancing Efficiency and Stability of Perovskite Solar Cells through Nb-Doping of TiO_2 at Low Temperature. *ACS Appl. Mater. Interfaces* **2017**, *9*, 10752−10758.

(18) Pang, S. P.; Hu, H.; Zhang, J. L.; Lv, S. L.; Yu, Y. M.; Wei, F.; Qin, T. S.; Xu, H. X.; Liu, Z. H.; Cui, G. L. $NH_2CH=NH_2PbI_3$: An Alternative Organolead Iodide Perovskite Sensitizer for Mesoscopic Solar Cells. *Chem. Mater.* **2014**, *26*, 1485−1491.

(19) Yang, W. S.; Noh, J. H.; Jeon, N. J.; Kim, Y. C.; Ryu, S.; Seo, J.; Seok, S. I. High-Performance Photovoltaic Perovskite Layers Fabricated through Intramolecular Exchange. *Science* **2015**, *348*, 1234−1237.

(20) Zong, Y. X.; Wang, N.; Zhang, L.; Ju, M. G.; Zeng, X. C.; Sun, X. W.; Zhou, Y.; Padture, N. P. Homogenous Alloys of Formamidinium Lead Triiodide and Cesium Tin Triiodide for Efficient Ideal-Bandgap Perovskite Solar Cells. *Angew. Chem., Int. Ed.* **2017**, *56*, 12658−12662.

(21) Liu, T. H.; Zong, Y. X.; Zhou, Y. Y.; Yang, M. J.; Li, Z.; Game, O. S.; Zhu, K.; Zhu, R.; Gong, Q. H.; Padture, N. P. High-Performance Formamidinium-Based Perovskite Solar Cells via Microstructure-Mediated delta-to-alpha Phase Transformation. *Chem. Mater.* **2017**, *29*, 3246−3250.

(22) Yang, W. S.; Park, B. W.; Jung, E. H.; Jeon, N. J.; Kim, Y. C.; Lee, D. U.; Shin, S. S.; Seo, J.; Kim, E. K.; Noh, J. H.; et al. Iodide Management in Formamidinium-Lead-Halide-based Perovskite Layers for Efficient Solar Cells. *Science* **2017**, *356*, 1376−1379.

(23) Kojima, A.; Teshima, K.; Shirai, Y.; Miyasaka, T. Organometal Halide Perovskites as Visible-Light Sensitizers for Photovoltaic Cells. *J. Am. Chem. Soc.* **2009**, *131*, 6050.

(24) Yang, D.; Yang, R. X.; Ren, X. D.; Zhu, X. J.; Yang, Z.; Li, C.; Liu, S. Z. Hysteresis-Suppressed High-Efficiency Flexible Perovskite Solar Cells Using Solid-State Ionic-Liquids for Effective Electron Transport. *Adv. Mater.* **2016**, *28*, 5206−5213.

(25) Levchuk, I.; Osvet, A.; Tang, X. F.; Brandl, M.; Perea, J. D.; Hoegl, F.; Matt, G. J.; Hock, R.; Batentschuk, M.; Brabec, C. J. Brightly Luminescent and Color-Tunable Formamidinium Lead Halide Perovskite $FAPbX_3$ (X = Cl, Br, I) Colloidal Nanocrystals. *Nano Lett.* **2017**, *17*, 2765−2770.

(26) Nagaoka, Y.; Hills-Kimball, K.; Tan, R.; Li, R.; Wang, Z.; Chen, O. Nanocube Superlattices of Cesium Lead Bromide Perovskites and

DOI: 10.1021/acs.jpclett.8b01852
J. Phys. Chem. Lett. 2018, 9, 4199−4205

Pressure-Induced Phase Transformations at Atomic and Mesoscale Levels. *Adv. Mater.* **2017**, *29*, 1606666.
(27) Zhu, H.; Nagaoka, Y.; Hills-Kimball, K.; Tan, R.; Yu, L.; Fang, Y.; Wang, K.; Li, R.; Wang, Z.; Chen, O. Pressure-Enabled Synthesis of Hetero-Dimers and Hetero-Rods through Intraparticle Coalescence and Interparticle Fusion of Quantum-Dot-Au Satellite Nanocrystals. *J. Am. Chem. Soc.* **2017**, *139*, 8408−8411.
(28) Wang, Z. W.; Chen, O.; Cao, C. Y.; Finkelstein, K.; Smilgies, D. M.; Lu, X. M.; Bassett, W. A. Integrating in situ High Pressure Small and Wide Angle Synchrotron X-ray Scattering for Exploiting New Physics of Nanoparticle Supercrystals. *Rev. Sci. Instrum.* **2010**, *81*, 093902.
(29) Li, B.; Bian, K.; Zhou, X.; Lu, P.; Liu, S.; Brener, I.; Sinclair, M.; Luk, T.; Schunk, H.; Alarid, L.; et al. Pressure Compression of CdSe Nanoparticles into Luminescent Nanowires. *Sci. Adv.* **2017**, *3*, e1602916.
(30) Li, B. S.; Bian, K. F.; Lane, J. M. D.; Salerno, K. M.; Grest, G. S.; Ao, T.; Hickman, R.; Wise, J.; Wang, Z. W.; Fan, H. Y. Superfast Assembly and Synthesis of Gold Nanostructures using Nanosecond Low-Temperature Compression via Magnetic Pulsed Power. *Nat. Commun.* **2017**, *8*, 15574.
(31) Bian, K. F.; Singh, A. K.; Hennig, R. G.; Wang, Z. W.; Hanrath, T. The Nanocrystal Superlattice Pressure Cell: A Novel Approach To Study Molecular Bundles under Uniaxial Compression. *Nano Lett.* **2014**, *14*, 4763−4766.
(32) Bian, K. F.; Richards, B. T.; Yang, H. Q.; Bassett, W.; Wise, F. W.; Wang, Z. W.; Hanrath, T. Optical Properties of PbS Nanocrystal Quantum Dots at Ambient and Elevated Pressure. *Phys. Chem. Chem. Phys.* **2014**, *16*, 8515−8520.
(33) Wang, T.; Li, R. P.; Quan, Z. W.; Loc, W. S.; Bassett, W. A.; Xu, H. W.; Cao, Y. C.; Fang, J. Y.; Wang, Z. W. Pressure Processing of Nanocube Assemblies Toward Harvesting of a Metastable PbS Phase. *Adv. Mater.* **2015**, *27*, 4544−4549.
(34) Li, R. P.; Bian, K. F.; Hanrath, T.; Bassett, W. A.; Wang, Z. W. Decoding the Superlattice and Interface Structure of Truncate PbS Nanocrystal-Assembled Supercrystal and Associated Interaction Forces. *J. Am. Chem. Soc.* **2014**, *136*, 12047−12055.
(35) Huang, X. J.; Yang, W. G.; Harder, R.; Sun, Y. G.; Lu, M.; Chu, Y. S.; Robinson, I. K.; Mao, H. K. Deformation Twinning of a Silver Nanocrystal under High Pressure. *Nano Lett.* **2015**, *15*, 7644−7649.
(36) Yin, T. T.; Fang, Y. N.; Chong, W. K.; Ming, K. T.; Jiang, S. J.; Li, X. L.; Kuo, J. L.; Fang, J. Y.; Sum, T. C.; White, T. J. High-Pressure-Induced Comminution and Recrystallization of $CH_3NH_3PbBr_3$ Nanocrystals as Large Thin Nanoplates. *Adv. Mater.* **2018**, *30*, 1705017.
(37) Liu, G.; Kong, L. P.; Gong, J.; Yang, W. G.; Mao, H. K.; Hu, Q. Y.; Liu, Z. X.; Schaller, R. D.; Zhang, D. Z.; Xu, T. Pressure-Induced Bandgap Optimization in Lead-Based Perovskites with Prolonged Carrier Lifetime and Ambient Retainability. *Adv. Funct. Mater.* **2017**, *27*, 1604208.
(38) Lu, X. J.; Wang, Y. G.; Stoumpos, C. C.; Hu, Q. Y.; Guo, X. F.; Chen, H. J.; Yang, L. X.; Smith, J. S.; Yang, W. G.; Zhao, Y. S.; et al. Enhanced Structural Stability and Photo Responsiveness of $CH_3NH_3SnI_3$ Perovskite via Pressure-Induced Amorphization and Recrystallization. *Adv. Mater.* **2016**, *28*, 8663−8668.
(39) Li, Q.; Wang, Y. G.; Pan, W. C.; Yang, W. G.; Zou, B.; Tang, J.; Quan, Z. W. High-Pressure Band-Gap Engineering in Lead-Free Cs2AgBiBr6 Double Perovskite. *Angew. Chem., Int. Ed.* **2017**, *56*, 15969−15973.
(40) Jaffe, A.; Lin, Y.; Beavers, C. M.; Voss, J.; Mao, W. L.; Karunadasa, H. I. High-Pressure Single-Crystal Structures of 3D Lead-Halide Hybrid Perovskites and Pressure Effects on their Electronic and Optical Properties. *ACS Cent. Sci.* **2016**, *2*, 201−209.
(41) Jiang, S. J.; Fang, Y. A.; Li, R. P.; Xiao, H.; Crowley, J.; Wang, C. Y.; White, T. J.; Goddard, W. A.; Wang, Z. W.; Baikie, T.; et al. Pressure-Dependent Polymorphism and Band-Gap Tuning of Methylammonium Lead Iodide Perovskite. *Angew. Chem., Int. Ed.* **2016**, *55*, 6540−6544.
(42) Jaffe, A.; Lin, Y.; Karunadasa, H. I. Halide Perovskites under Pressure: Accessing New Properties through Lattice Compression. *ACS Energy Lett.* **2017**, *2*, 1549−1555.
(43) Lu, X. J.; Yang, W. G.; Jia, Q. X.; Xu, H. W. Pressure-Induced Dramatic Changes in Organic-Inorganic Halide Perovskites. *Chem. Sci.* **2017**, *8*, 6764−6776.
(44) Cao, Y.; Qi, G. Y.; Liu, C.; Wang, L. R.; Ma, Z. W.; Wang, K.; Du, F.; Xiao, G. J.; Zou, B. Pressure-Tailored Band Gap Engineering and Structure Evolution of Cubic Cesium Lead Iodide Perovskite Nanocrystals. *J. Phys. Chem. C* **2018**, *122*, 9332−9338.
(45) Wang, L. R.; Wang, K.; Zou, B. Pressure-Induced Structural and Optical Properties of Organometal Halide Perovskite-Based Formamidinium Lead Bromide. *J. Phys. Chem. Lett.* **2016**, *7*, 2556−2562.
(46) Wang, P.; Guan, J. W.; Galeschuk, D. T. K.; Yao, Y. S.; He, C. F.; Jiang, S.; Zhang, S. J.; Liu, Y.; Jin, M. L.; Jin, C. Q.; et al. Pressure-Induced Polymorphic, Optical, and Electronic Transitions of Formamidinium Lead Iodide Perovskite. *J. Phys. Chem. Lett.* **2017**, *8*, 2119−2125.
(47) Dabbousi, B. O.; Murray, C. B.; Rubner, M. F.; Bawendi, M. G. Langmuir-Blodgett Manipulation of Size-Selected Cdse Nanocrystallites. *Chem. Mater.* **1994**, *6*, 216−219.
(48) Hills-Kimball, K.; Nagaoka, Y.; Cao, C.; Chaykovsky, E.; Chen, O. Synthesis of Formamidinium Lead Halide Perovskite Nanocrystals through Solid-Liquid-Solid Cation Exchange. *J. Mater. Chem. C* **2017**, *5*, 5680−5684.
(49) Motta, C.; El-Mellouhi, F.; Sanvito, S. Exploring the cation dynamics in lead-bromide hybrid perovskites. *Phys. Rev. B: Condens. Matter Mater. Phys.* **2016**, *93*, 235412.
(50) Zhumekenov, A. A.; Saidaminov, M. I.; Haque, M. A.; Alarousu, E.; Sarmah, S. P.; Murali, B.; Dursun, I.; Miao, X. H.; Abdelhady, A. L.; Wu, T.; et al. Formamidinium Lead Halide Perovskite Crystals with Unprecedented Long Carrier Dynamics and Diffusion Length. *ACS Energy Lett.* **2016**, *1*, 32−37.
(51) Xiao, G. J.; Cao, Y.; Qi, G. Y.; Wang, L. R.; Liu, C.; Ma, Z. W.; Yang, X. Y.; Sui, Y. M.; Zheng, W. T.; Zou, B. Pressure Effects on Structure and Optical Properties in Cesium Lead Bromide Perovskite Nanocrystals. *J. Am. Chem. Soc.* **2017**, *139*, 10087−10094.
(52) Swainson, I. P.; Tucker, M. G.; Wilson, D. J.; Winkler, B.; Milman, V. Pressure Response of an Organic-Inorganic Perovskite: Methylammonium Lead Bromide. *Chem. Mater.* **2007**, *19*, 2401−2405.
(53) Lee, Y.; Mitzi, D. B.; Barnes, P. W.; Vogt, T. Pressure-Induced Phase Transitions and Templating Effect in Three-Dimensional Organic-Inorganic Hybrid Perovskites. *Phys. Rev. B: Condens. Matter Mater. Phys.* **2003**, *68*, 020103.
(54) Glazer, A. M. The Classification of Tilted Octahedra in Perovskites. *Acta Crystallogr., Sect. B: Struct. Crystallogr. Cryst. Chem.* **1972**, *28*, 3384−3392.
(55) Manser, J. S.; Saidaminov, M. I.; Christians, J. A.; Bakr, O. M.; Kamat, P. V. Making and Breaking of Lead Halide Perovskites. *Acc. Chem. Res.* **2016**, *49*, 330−338.
(56) Tian, Y. X.; Merdasa, A.; Unger, E.; Abdellah, M.; Zheng, K. B.; McKibbin, S.; Mikkelsen, A.; Pullerits, T.; Yartsev, A.; Sundstrom, V.; et al. Enhanced Organo-Metal Halide Perovskite Photoluminescence from Nanosized Defect-Free Crystallites and Emitting Sites. *J. Phys. Chem. Lett.* **2015**, *6*, 4171−4177.
(57) Giannozzi, P.; Andreussi, O.; Brumme, T.; Bunau, O.; Buongiorno Nardelli, M.; Calandra, M.; Car, R.; Cavazzoni, C.; Ceresoli, D.; Cococcioni, M.; et al. Advanced Capabilities for Materials Modelling with QUANTUM ESPRESSO. *J. Phys.: Condens. Matter* **2017**, *29*, 465901−465931.
(58) Liechtenstein, A. I.; Anisimov, V. I.; Zaanen, J. Density-Functional Theory and Strong-Interactions - Orbital Ordering in Mott-Hubbard Insulators. *Phys. Rev. B: Condens. Matter Mater. Phys.* **1995**, *52*, R5467−R5470.
(59) Dudarev, S. L.; Botton, G. A.; Savrasov, S. Y.; Humphreys, C. J.; Sutton, A. P. Electron-Energy-Loss Spectra and the Structural Stability of Nickel Oxide: An LSDA+U Study. *Phys. Rev. B: Condens. Matter Mater. Phys.* **1998**, *57*, 1505−1509.

DOI: 10.1021/acs.jpclett.8b01852
J. Phys. Chem. Lett. 2018, 9, 4199−4205